Sensors & Actuators: B. Chemical 357 (2022) 131359

Contents lists available at ScienceDirect

Sensors and Actuators: B. Chemical

journal homepage: www.elsevier.com/locate/snb

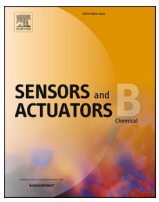

In-situ synthesized N-doped ZnO for enhanced CO_2 sensing: Experiments and DFT calculations

Yong Xia [a,b,c,d], Aifei Pan [a,b,c,d], Ya-Qiong Su [e,f], Sikai Zhao [c,d,g], Zhou Li [c,d], Adrian K. Davey [c,d], Libo Zhao [a,b,*], Roya Maboudian [c,d,**], Carlo Carraro [c,d,**]

[a] State Key Laboratory for Manufacturing Systems Engineering, International Joint Laboratory for Micro/Nano Manufacturing and Measurement Technologies, Overseas Expertise Introduction Center for Micro/Nano Manufacturing and Nano Measurement Technologies Discipline Innovation, Xi'an Jiaotong University (Yantai) Research Institute for Intelligent Sensing Technology and System, Xi'an Jiaotong University, Xi'an 710054, China
[b] School of Mechanical Engineering, Xi'an Jiaotong University, Xi'an 710049, China
[c] Department of Chemical and Biomolecular Engineering, University of California, Berkeley, CA 94720, United States
[d] Berkeley Sensor & Actuator Center, University of California, Berkeley, CA 94720, United States
[e] School of Chemistry, Xi'an Key Laboratory of Sustainable Energy Materials Chemistry, State Key Laboratory of Electrical Insulation and Power Equipment, Xi'an Jiaotong University, Xi'an 710049, China
[f] Laboratory of Inorganic Materials & Catalysis, Schuit Institute of Catalysis, Eindhoven University of Technology, P.O. Box 513, 5600 MB Eindhoven, The Netherlands
[g] School of Resources and Civil Engineering, Northeastern University, Shenyang 110819, China

ARTICLE INFO

Keywords:
In-situ annealing
N-doped ZnO
CO_2 sensing
Mechanism study
DFT calculation

ABSTRACT

Chemiresistive CO_2 sensing is attractive due to low cost and ease of chip-level integration. Our previous studies (Yong Xia, 2021) showed the well-developed ZnO material fabricated by in-situ annealing exhibited good CO_2 sensing performance. Here, we have expanded on those studies, including CO_2 cyclic tests under both dry air and N_2 background whereby a much higher response to CO_2 in N_2 background was observed. Detailed density functional theory calculations were conducted to understand the behavior. The results indicated nitrogen doping is mainly responsible for the observed response. In the presence of pre-adsorbed O_2, N-doped ZnO can no longer interact with CO_2, which agrees well with the observation of higher response in N_2 background. Furthermore, density of states analysis showed N sp^2 hybridized orbital and N 2p orbital of the N dopant mixed with sp^2 hybridized orbital of C atom and 2p orbitals of C/O atoms in CO_2 to form σ and π bonds, respectively. However, they mixed with O 2s/2p orbitals of O atom in O_2 when pre-adsorbed O_2 was present, hindering CO_2 interaction with N-doped ZnO, and resulting in limited response in air. The illustrated mechanism does not only further the understanding of metal oxide-based CO_2 sensing, but also guide the design of new functional materials for CO_2 sensing or capture.

1. Introduction

Carbon dioxide sensing is of great importance for indoor air quality control [1], green house agriculture [2], factory emission surveillance [3], and breath clinical diagnostics [4]. Currently, there are mainly four types of CO_2 sensors: nondispersive infrared (NDIR) sensors [5], solid state electrochemical sensors [6], gravimetric sensors [7], and semiconductor-based chemiresistive sensors [8,9]. Among these, chemiresistive sensors have attracted great interests due to their simple structures and readout circuits, ease of fabrication and chip integration, as well as low cost.

Since CO_2 is chemically inert, traditional redox reaction based chemiresistive sensors exhibit limited sensitivity, and some researchers are exploring carbonation process-induced resistance change [10–12].

* Corresponding author at: State Key Laboratory for Manufacturing Systems Engineering, International Joint Laboratory for Micro/Nano Manufacturing and Measurement Technologies, Overseas Expertise Introduction Center for Micro/Nano Manufacturing and Nano Measurement Technologies Discipline Innovation, Xi'an Jiaotong University (Yantai) Research Institute for Intelligent Sensing Technology and System, Xi'an Jiaotong University, Xi'an 710054, China
** Corresponding authors at: Department of Chemical and Biomolecular Engineering, University of California, Berkeley,CA 94720, United States.
E-mail addresses: xia395714753@stu.xjtu.edu.cn (Y. Xia), aifeipan@stu.xjtu.edu.cn (A. Pan), yqsu1989@xjtu.edu.cn (Y.-Q. Su), zhaosikai@stumail.neu.edu.cn (S. Zhao), zhouli@berkeley.edu (Z. Li), adavey1@berkeley.edu (A.K. Davey), libozhao@mail.xjtu.edu.cn (L. Zhao), maboudia@berkeley.edu (R. Maboudian), carraro@berkeley.edu (C. Carraro).

https://doi.org/10.1016/j.snb.2022.131359
Received 15 October 2021; Received in revised form 7 December 2021; Accepted 1 January 2022
Available online 4 January 2022

For example, Joshi et al. synthesized Ag@CuO/$BaTiO_3$ and achieved more than 6-fold higher response than the pure CuO counterparts by heterojunction modulation during CO_2 sensing [10]. Though big processes have been made, the heterojunction structure increases the difficulty in material design and synthesis. In addition, the sensing response needs to be further improved.

Recent studies have shown that rare-earth oxides and oxycarbonates, especially $La_2O_2CO_3$, can react with CO_2 directly to form surface carbonates/oxycarbonates and exhibit a high CO_2 response which opens up a new opportunity for CO_2 monitoring [8,9,13]. However, rare-earth materials are relatively expensive, and their ability for monitoring other ubiquitous gases (such as C_2H_5OH, H_2S, CH_2O, etc.) is still needed to be verified. The well-developed semiconducting materials, such as ZnO, SnO_2, and WO_3, though insufficient in selectivity, can serve as a low-cost sensing "base-material" for a variety of gases. Thus, it would be more preferable in industrial production to use these materials since similar basic properties of sensing materials would greatly simplify the mass production process of the gas sensors for various gases sensing. Therefore, developing a new material for CO_2 sensing based on these well-developed materials is a worthwhile challenge to undertake.

From our previous work [14], the in-situ annealed ZnO exhibited much higher selectivity to CO_2 than the ex-situ annealed counterpart. To understand the CO_2 sensing mechanism, here, a new in-situ annealed device was fabricated and the dynamic CO_2 sensing properties in both air and N_2 background were evaluated. Surface models for density function theory (DFT) calculation were constructed on the basis of the differences in the X-ray photoelectron spectroscopy results obtained on the in-situ annealed material and the ex-situ annealed counterpart. Based on the calculations, CO_2 adsorption features were systematically studied and compared among different surface models. Finally, the CO_2 sensing mechanism of the in-situ annealed ZnO was clearly elucidated by combining the gas sensing results and the DFT calculations.

2. Experiments

2.1. Chemicals

Chemicals of Zinc Acetate Dihydrate (Zn $(CH_3COO)_2{\cdot}2H_2O$, analytically pure), 2-methylimidazolate (2-MIM, $C_4H_6N_2$, 99%), and Cetyl Trimethyl Ammonium Bromide (CTAB, $C_{19}H_{42}BrN$, >98%) were purchased from Sigma Aldrich and used directly without further purification.

2.2. Materials synthesis and sensor fabrication

The material synthesis and sensor fabrication process are described in our previous work [14]. Typically, 130 μl 4 mg/ml of CTAB aqueous solution was added to 5 ml 240 mg/ml of 2-MIM aqueous solution and mixed with 5 ml 60 mg/ml of $Zn(CH_3COO)_2.2H_2O$ aqueous solution in an iced water bath. After mixing, the solution was taken out and settled down for 2 h. Then, the milky solution was centrifuged and washed with DI water. And the obtained white material was dispersed in 1-butanol solution for further usage.

The sensor was fabricated by in-situ heating the drop-casted ZIF-8 film using a miniature heater electrode (Alite Technology Co., Ltd., Beijing, China) at 350 ℃ for 2 h with a ramp rate of 60 ℃/s. The sensor is denoted as "in-situ annealed sensor".

2.3. Material characterizations

The field-emission scanning electron microscopy (FESEM, Zeiss Ultra 55) and the transmission electron microscopy (HRTEM, JEOL 2100 F) was used to characterize the morphology of the materials. EDAX spectrum was obtained using an EDAX TEAM with operating voltage 15 kV assembled in a FESEM (SU8010, Hitachi, Japan) to characterize elements in the materials. X-ray diffraction (XRD, Bruker AXS D8 Discover GADDS, $\lambda_{Co} = 0.179$ nm) was used to characterized the crystal structures of the as-synthesized materials. The XRD spectra shown here were transformed into Cu Kα. Raman spectroscopy (JYHoriba LabRAM) were used to characterize the surface chemical states and chemical bonding structures of the as-synthesized materials, respectively.

2.4. Gas sensing measurement

The sensor packaged with a ceramic chip holder was fixed on an IC test socket which was covered by a home-made gas chamber (1 cm^3 volume size). CO_2 (Airgas, 5.038% in N_2) was mixed with dry air or N_2 (Praxair, 99.999%) with a constant total flowrate of 300 sccm and delivered by mass flow controllers (Bronkhurst). The lowest concentration that our gas delivery system can reliably deliver is 50 ppm CO_2. The background atmospheres are denoted as "air background" and "N_2 background" when CO_2 is diluted by dry air and N_2, respectively. The gas delivery system was controlled by a home-made LabVIEW program. The sensor resistance was measured by a source-meter (Keithley 2602 A) and recorded by an open-source Java based measurement software of Zephyr.

2.5. DFT calculations

All of the calculations were performed using Vienna ab initio Simulation Package (VASP) [15,16]. The projector augmented wave (PAW) method with a cut-off energy of 450 eV was used to describe the interactions of electrons and ion cores. Generalized gradient approximation (GGA) proposed by Perdew-Burke-Ernzerhof (PBE) [17] was applied to describe exchange-correlation potential of the electrons.

The molecular CO_2 was pre-relaxed in a cubic box of 20 × 20.01 × 20.02 $Å^3$ to avoid symmetry induced degeneration [18] and interactions among different image cells [19]. During CO_2 molecule relaxation and energy calculations, only Gamma point for Brillouin zone (BZ) integrations was considered. The slab models were built in the part of "Modeling of surfaces" in Supplementary Materials. For relaxation and total energy calculations of slabs and slabs/CO_2 systems, the Gamma centered k-mesh of 3 × 3 × 1 was applied. For structure optimization, the convergence criterion of energy and force on each atom were 1×10^{-5} eV and 0.01 eV/Å, respectively. Higher convergence criterion of 10^{-6} eV/atom was used for density of state (DOS) calculations.

To correct the long-range van der Waals force between the gas molecules and the slab surfaces during the surface adsorption processes, DFT-D3 correction proposed by Grimme et al.[20] was applied during calculation of CO_2/slab interactions.

The gas adsorption status was assessed by its adsorption energy E_{abs}, which can be calculated as:

$$E_{ads} = E_{slab-CO_2} - E_{slab} - E_{CO_2} \quad (1)$$

where $E_{slab\text{-}CO2}$, E_{slab} and E_{CO2} are the energies of the slab/CO_2, slab and CO_2 systems, respectively.

The charge density difference (CDD) was also calculated and visualized by VESTA code [21] to exhibit the charge distributions after gas adsorptions. The CDD can be determined by following equations:

$$\Delta\rho = \rho_{slab-CO_2} - \rho_{slab} - \rho_{CO_2} \quad (2)$$

where $\rho_{slab\text{-}CO2}$, ρ_{slab}, ρ_{CO2} are charge density of the slab/CO_2, slab and CO_2 systems, respectively.

In addition, the Bader charge [22] was calculated to evaluate the charge transfer between the slabs and CO_2 molecule using the method developed by Henkelman group [23], where the positive value indicates the slab obtain electrons from CO_2 molecule.

3. Results and discussion

3.1. Material characterization

The morphology of the as-synthesized ZnO material is shown in Fig. 1. The material appears as a porous network consisting of connected nanoparticles, as shown in Fig. 1(a). The transmission electron microscopy (TEM) image in Fig. 1(b) shows that the nanoparticles are solid particles and tightly connected with each other. The high resolution TEM image along with a diffraction pattern in the insets of Fig. 1(b) show two main lattice spacings of 0.260 nm and 0.248 nm in the particle connecting areas which correspond to (002) and (101) facets of hexagonal ZnO, respectively. The EDX spectrum of the material in Fig. 1(c) indicates the material contains elements of C, N, O and Zn, with the concentration of nitrogen being small agrees with our previous results [14].

The crystal structure of the as-synthesized material is shown in Fig. 2 (a). Apart from Al_2O_3 peaks from the ceramic substrate and Au peaks of the sensing electrodes, the diffraction pattern clearly shows the as-synthesized material is hexagonal wurtzite ZnO.

To understand the chemical bonding and defect states of the as-synthesized ZnO, Raman spectroscopy was used with representative results shown in Fig. 2(b). The peaks at 333 and 438 cm^{-1} Raman shift are attributed to the combination mode (E_2(high)-E_2(low)) and to the E_2(high) mode of hexagonal ZnO, respectively [24]. The broad peak at 580 cm^{-1} is attributed to "Quasi-LO" mode consisting of A_1(LO) and E_1(LO) modes. This mode is attributed to inter-band Frohlich interaction in non-ideal ZnO, and its appearance usually indicates donor defects, e.g., oxygen vacancy (V_O), and interstitial Zn (Zn_i) of ZnO [25]. Additionally, the peak at 235 cm^{-1} is probably attributed to a kind of defect mode since it is not visible in an ideal ZnO crystal [26].

The material characterization above indicates the as-prepared material is well-connected ZnO nanoparticle network with donor defects, which is similar as our previous work [14]. Therefore, the chemical nature of the surface is also believed to be similar to that studied in our previous work (shown in Fig. S1).

3.2. Gas sensing performance in dry air and N_2 background

To understand the CO_2 sensing mechanism, the sensor was first tested under N_2 background. The result is shown in Fig. 3(a, b). Interestingly, the sensor resistance upon CO_2 exposure during this stabilization period is almost constant, while the baseline is changing quickly, as indicated by 2 horizontal lines of "100 ppm" and "500 ppm" in the Fig. 3 (a). The CO_2 sensing ability in N_2 background indicates the CO_2 response mechanism is independent of pre-adsorbed O_2 which is different from most recently developed CO_2 sensing materials [8,27,28]. Fig. 3(b) is CO_2 cycling result after N_2 purging for 90 min at which point the baseline becomes relatively stable. It is shown the sensor exhibits reasonable responses to different concentrations of CO_2. The response behavior is stable and reproducible.

Fig. 3(c) shows the sensor response to CO_2 exposure cycles under air background where the gas sensing performance is commonly evaluated. Similar to N_2 background, the response to CO_2 in the air background is also stable and reproducible. The baseline resistance in the air background is 20x larger than in the N_2 background. The higher resistance can be attributed to O_2 adsorption induced electron depletion in the air background, which exhibits n-type semiconductor behavior of the sensing material. The adsorbed oxygen species are estimated as O^{2-} and O^- with the O^{2-} being dominant, according to the log-log plot shown in Fig. S4.

Fig. 3(d) is the plot of sensor response versus CO_2 concentration when testing in air and N_2 background. The results indicate higher responses are obtained when testing in the N_2 background than in the air background. The higher responses in N_2 background indicates that far from accelerating CO_2-sensing material interaction, O_2 in the air inhibits the process.

To explore how the sensing material changes during CO_2 exposures, the material was characterized ex-situ with XRD before and after a cyclic test of 5000 ppm CO_2 at 250 °C (air background). The results shown in Fig. S5 exhibit similar peaks as the spectrum in Fig. 2, which indicates the materials, as probed by XRD, are the same. No obvious peak differences are found after CO_2 sensing which indicates no major changes happen to the base ZnO material. Therefore, the following discussions focus on the surface interactions.

3.3. DFT calculations

3.3.1. CO_2-surfaces interactions

To investigate various possible chemical states of the sensing material, a series of surface slabs, including stoichiometric wurtzite ZnO(101) (denoted as ZnO(101)), oxygen vacancy defective ZnO(101) (denoted as V_O-ZnO(101)), nitrogen doped ZnO(101) (denoted as N-ZnO(101)), N_2 substitution on oxygen sublattice of ZnO(101) (denoted as $(N_2)_O$-ZnO (101)) and oxidized N species on ZnO(101) (denoted as O-N-ZnO(101)) were built and calculated as shown in the "Modeling of surface" section of Supplementary Materials. The result indicates $(N_2)_O$-ZnO(101) is not stable. Therefore, only ZnO(101), V_O-ZnO(101), N-ZnO(101) and O-N-ZnO(101) will be considered in the following study of CO_2 adsorption.

To gain insight into the CO_2 sensing mechanism, CO_2 adsorption on these slabs was studied. The most energetically favorable adsorption structures for each slab are shown in Fig. 4(a–d). Only the 1st layer of the slab is shown for better observation of surface interactions. After adsorption, it is found that the CO_2 conformation remains linear in all

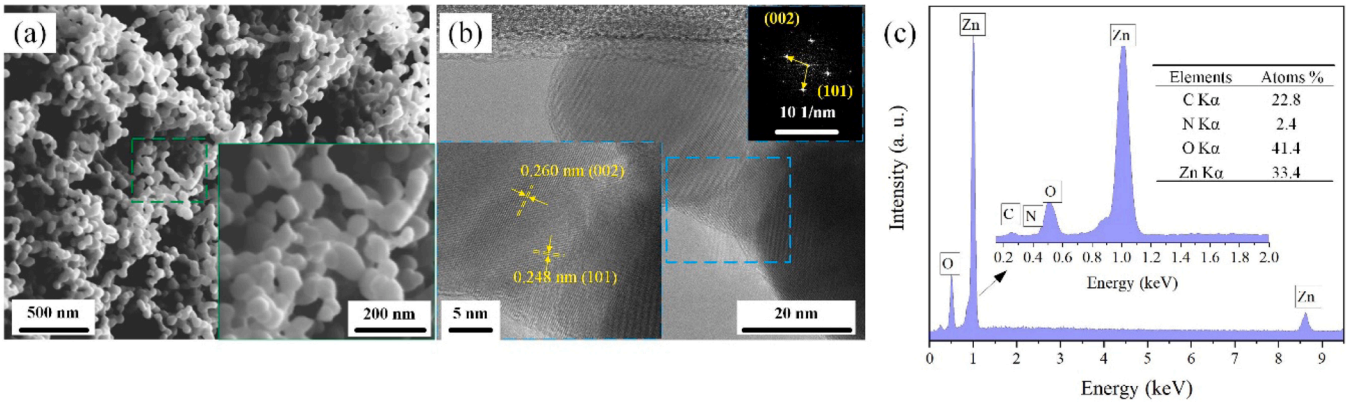

Fig. 1. Morphology of the sensing material. (a) Scanning electron microscopy image of the sensing material; (b) TEM image of the sensing material. The insets are the correspondingly enlarged parts and calculated diffraction pattern, respectively. (c) EDX spectrum of the material.

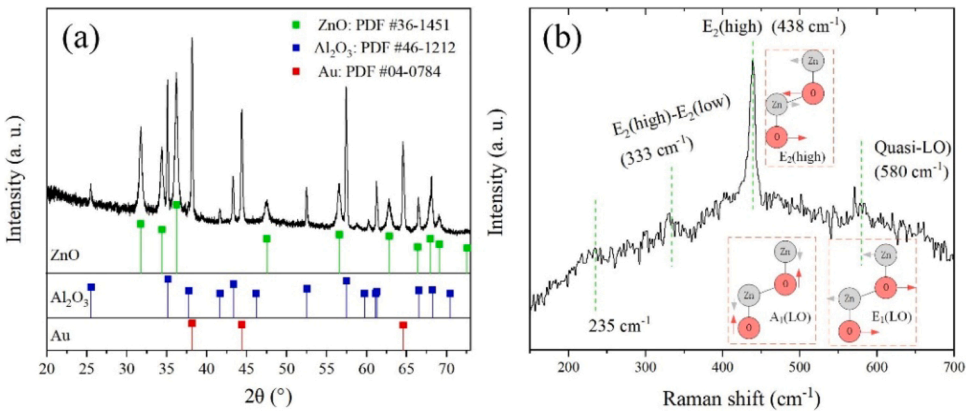

Fig. 2. Crystal structure and bonding characterizations of the sensing material. (a) X-ray diffraction pattern; (b) Raman spectrum.

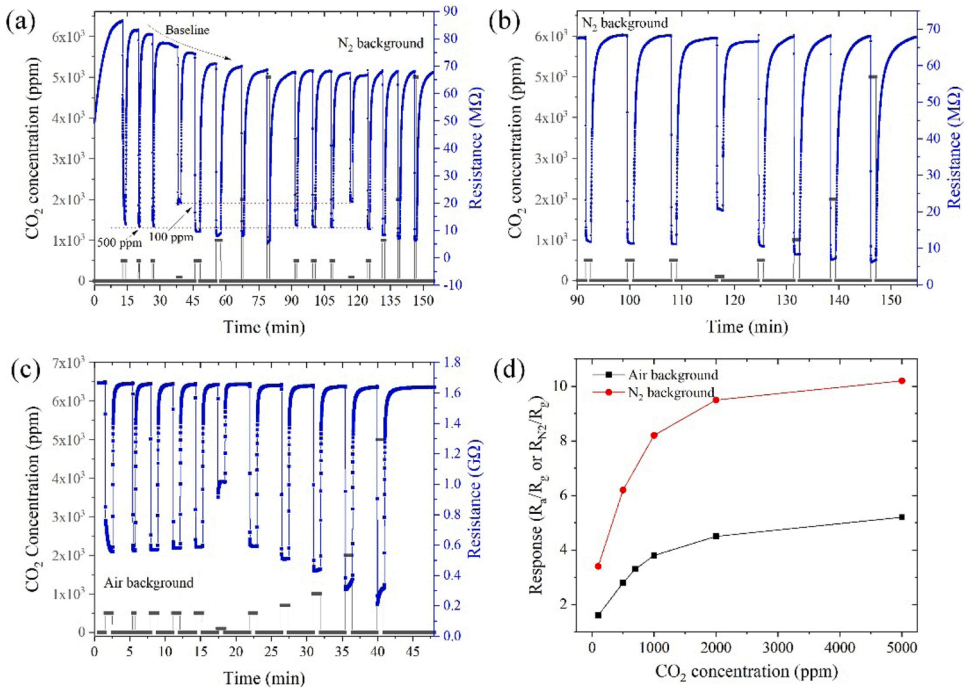

Fig. 3. Sensor response to cyclic CO_2 exposure at 250 °C. (a) under N_2 background as CO_2 is introduced; (b) under N_2 background after baseline resistance stabilizes; (c) under air background; (d) Response value vs. CO_2 concentration plot both in air and N_2 backgrounds.

cases except on N-ZnO(101), where the O-C-O bond angle is 124.29°. In addition, the nearest distance between the CO_2 molecule and the slab is the C-N distance of 1.35 Å, which is the similar length of C-N bonds in acrylic amide [29]. This indicates that CO_2 on N-ZnO(101) is chemisorbed (at a nitrogen site), while on ZnO(101), V_O-ZnO(101) and O-N-ZnO(101), it is physisorbed since the nearest distances between CO_2 and the slabs are far larger than the Zn-O bond length of 2.01 Å [30].

To understand the interactions between the slabs and CO_2, the charge difference density (CDD) upon CO_2 adsorption was studied. and shown in Fig. 4(e-h). For clarity, only the 1st layer and the 1st two layers of the slabs are shown in the top views and side views, respectively.

The charge density of ZnO(101) changes little upon CO_2 adsorption, and charge density isosurface is only seen on CO_2 molecule, as shown in Fig. 4(e), which indicates weak interactions. However, in the cases of CO_2 adsorption on V_O-ZnO(101), N-ZnO(101) and O-N-ZnO(101), the charge accumulation (in light yellow color) and depletion (in cyan color) regions overlap which indicate strong interactions between the slabs and CO_2 molecule. The charge isosurface regions show up far away from CO_2 molecule which indicates there exists a big charge reconstruction upon CO_2 adsorption on these slabs.

To further evaluate the interactions between the four slabs and CO_2 molecule, adsorption energy, Bader charge and electronic density of state (DOS) were calculated. The results of gas-slab interfacial distance ($d_{gas\text{-}slab}$), adsorption energy (E_{ads}), and Bader charge (ΔQ) are tabulated in Table 1. It is shown that N-ZnO(101) has the highest adsorption energy of −1.61 eV, in agreement with its chemisorption features. In addition, the charge transfer from CO_2 to N-ZnO is positive. It is worth noting that N-ZnO(101) is the only instance of positive charge transfer among the four slabs studied here. This feature agrees with the experimental observation of decrease in resistance when the sensor is exposed to CO_2 (see Fig. 3(b)).

The calculated DOSs of different CO_2 adsorption systems are shown in Fig. 5. The local density of states (LDOS) of adsorbed CO_2 (CO_2^{ads}) on ZnO(101), V_O-ZnO(101) and O-N-ZnO(101) are discrete peaks (such as, the lowest unoccupied molecular orbital, HOMO; the highest unoccupied molecular orbital, HOMO), corresponding to the molecular orbitals of CO_2 and indication of weak interactions between the molecule and the slabs. Still, the LDOS peaks of CO_2^{ads} on O-N-ZnO(101) and LUMO of

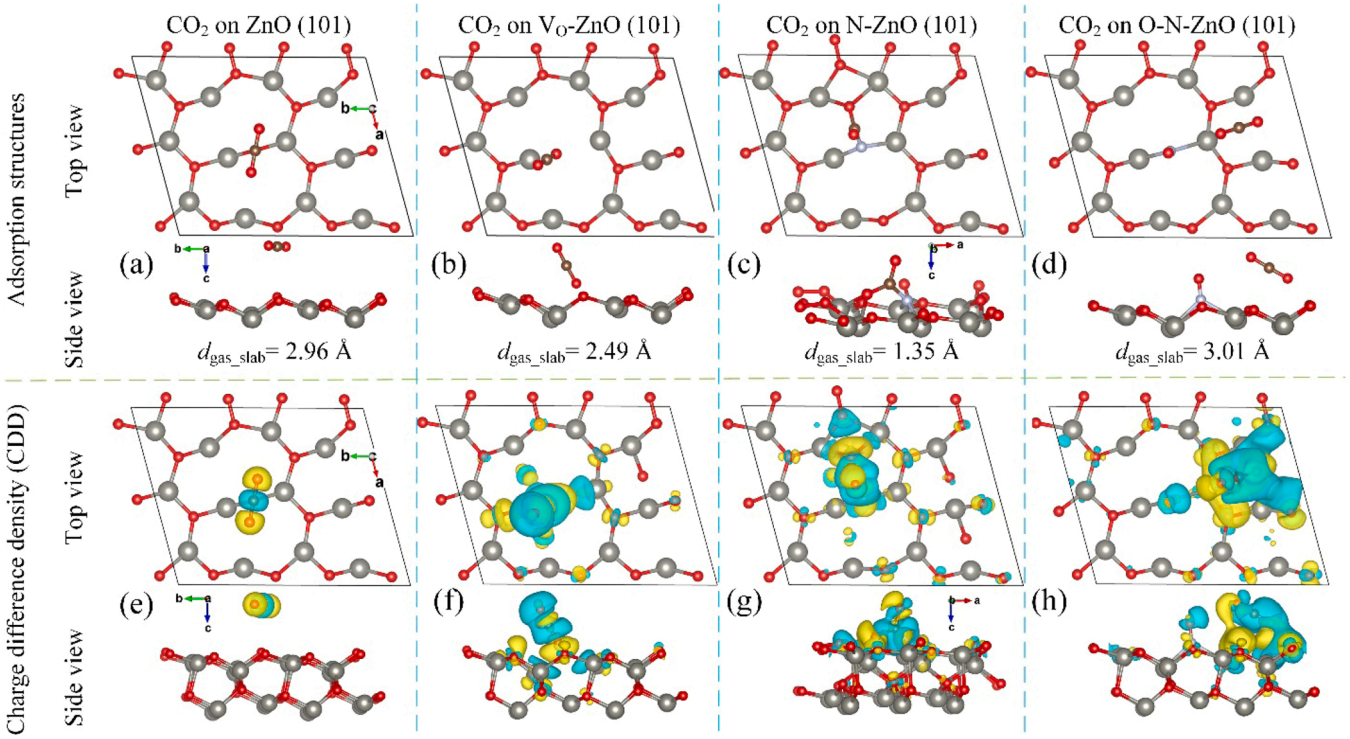

Fig. 4. CO_2 adsorption structures (a-d) and CDD (e-h) on different slabs with top views and side views. (a, e) CO_2 adsorption on ZnO(101); (b, f) CO_2 adsorption on V_O-ZnO(101); (c, g) CO_2 adsorption on N-ZnO(101); (d, h) CO_2 adsorption on O-N-ZnO(101). Isosurface levels are set 2.6×10^{-2} e/Bohr^3 for ZnO(101)-CO_2, 4.5×10^{-4} e/Bohr^3 for V_O-ZnO(101)-CO_2, 2.5×10^{-3} e/Bohr^3 for N-ZnO(101)-CO_2, and 1.4×10^{-4} e/Bohr^3 for O-N-ZnO(101)-CO_2. The default coordination above is the coordination in (a, e). The charge accumulation and depletion areas are shown in yellow and cyan, respectively. The red, gray, brown and white spheres correspond to O, Zn, C and N atoms, respectively. For clarity, only the 1st layer in the top views and the 1st layer or the 1st two layers in the side views are shown.

Table 1
Calculated gas-slab interfacial distance ($d_{gas\text{-}slab}$), adsorption energy (E_{ads}), and Bader charge of CO_2 adsorption on different slabs. Positive values of ΔQ represent CO_2 as an electron donor. All the adsorption energy and charge transfer values are calculated per CO_2 molecule.

Model	d_{gas_slab} (Å)	E_{abs} (eV)	ΔQ (e)[a]
ZnO(101)	2.96	0.01	-0.010
V_O-ZnO(101)	2.49	-0.60	-0.003
N-ZnO(101)	1.35	-1.61	0.019
O-N-ZnO(101)	3.01	-0.50	-0.017

[a] The higher resolution is applied due to small values.

CO_2^{ads} on V_O-ZnO(101) are broadened, and all of the orbitals shift to lower energy compared to the case of ZnO(101). All of these results indicate the interactions between CO_2 and corresponding slabs (V_O-ZnO (101) and O-N-ZnO(101)) are larger than with ZnO(101).

In the case of N-ZnO(101), the LDOSs of HOMO and LUMO of CO_2^{ads} are broadened and deeply mixed with the DOS of N-ZnO(101) slab, which are not easily discriminated. Instead, there exists a broad DOS around the Fermi energy, which is helpful in narrowing the bandgap of the slab and increasing the charge transfer probability [31]. The DOS results agree well with adsorption energy and Bader charge analysis, i.e., the interaction between CO_2/N-ZnO(101) is the strongest, CO_2/V_O-ZnO (101) and CO_2/O-N-ZnO(101) are moderate, while CO_2/ZnO(101) is the weakest.

In combine with the discussion above, considering that the in-situ annealed ZnO has higher concentration of N-Zn-O bond (~398.6 eV, Fig. S1), we thus believe the N-ZnO content in the in-situ annealed ZnO sensing materials is responsible for the CO_2 response features of the sensing material.

3.3.2. *CO_2-surfaces interactions with pre-adsorbed O_2*

To explain why the in-situ annealed ZnO showed higher responses in N_2 environment compared with air background, a comparative study of CO_2/N-ZnO(101) surface interactions with pre-adsorbed O_2 was conducted.

The optimized structure of O_2 pre-adsorbed N-ZnO(101) with the most preferable energy is shown in Fig. 6(a). One of the O atom in O_2 is close to the doped N atom, which is similar to the CO_2 adsorption structures shown in Fig. 4(c). The configuration of CO_2 adsorption on O_2 pre-adsorbed N-ZnO(101) is shown in Fig. 6(b), the bottom graph. It is clearly visible that after O_2 pre-adsorption, CO_2 can no longer approach the N-ZnO(101) surface. It is noted from the electron localization function (ELF) in Fig. 6(b, c) that both O_2 and CO_2 are chemisorbed on N-ZnO(101) at the site of doped N since shared electrons are found there [32].

To further understand the interaction features of CO_2 in the presence of O_2, the adsorption energy and Bader charge transfer of corresponding systems (O_2 adsorption on N-ZnO(101) and CO_2 adsorption on N-ZnO (101)-O_2) were calculated and the results, along with the data of CO_2 adsorption on N-ZnO(101) for comparison, are tabulated in Table 2. It is shown that O_2 has much higher adsorption energy than CO_2 on N-ZnO (101) (−3.50 eV vs. −1.61 eV), and the charge transfer amount is an order of magnitude bigger (−0.382 e vs. 0.019 e). Furthermore, when O_2 pre-adsorbed on N-ZnO(101), the CO_2 adsorption energy and charge transfer drop to −0.22 eV and −0.001 e, respectively.

Therefore, the weaker CO_2 response in air background can be explained as follows. When in the air background, O_2 preferentially adsorbs on N-ZnO(101) and saturates the lone pair electron of the nitrogen dopant. As a consequence, CO_2 has few bonding sites available, and thus the sensing response is lower than without background O_2. The large charge transfer difference between O_2 and CO_2 (−0.382 e vs. 0.019 e) could also explain why the "response resistance" is almost constant to the same concentration CO_2 pulses while the baseline decreases quickly

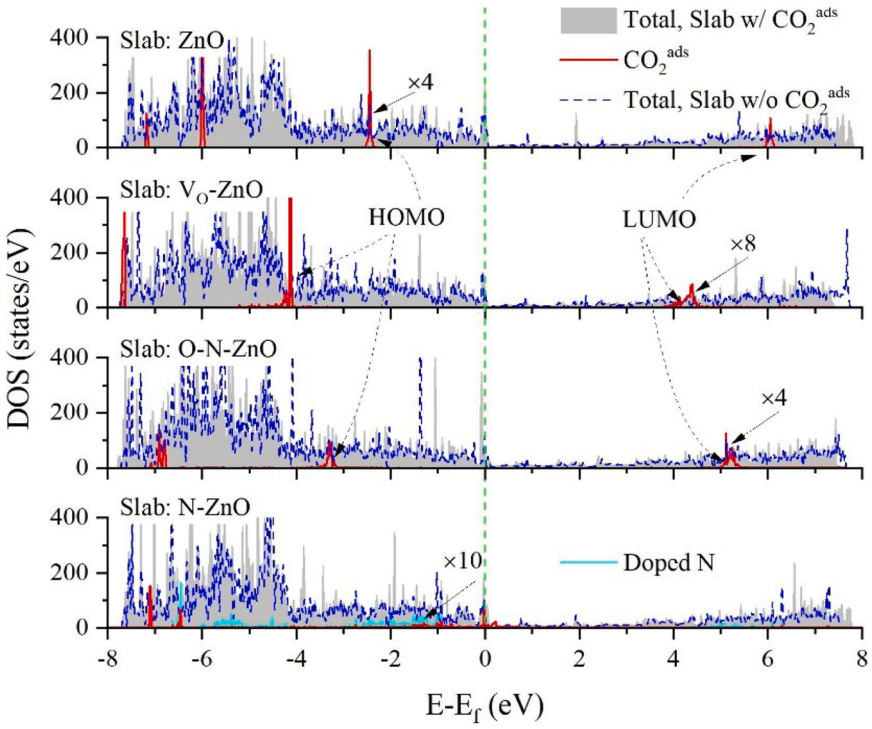

Fig. 5. Density of states analysis of CO_2 adsorption on different surfaces. For clarity, the DOSs of CO_2^{ads} and doped N are enlarged.

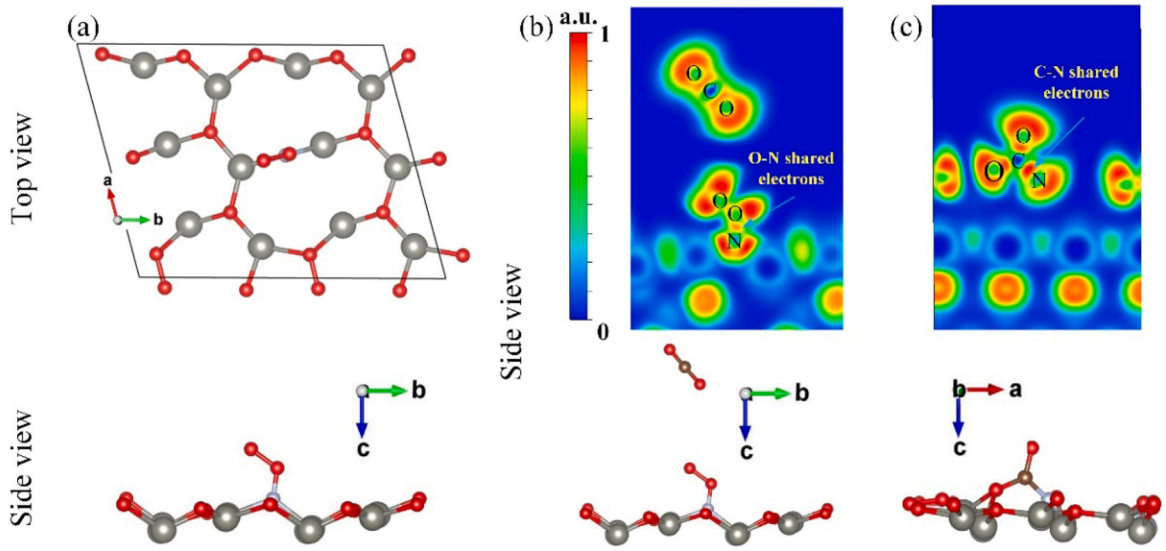

Fig. 6. Adsorption configurations of O_2 on N-ZnO(101) surface and CO_2 on O_2 pre-adsorbed N-ZnO(101) and their corresponding ELF maps. (a) O_2 adsorption on N-ZnO; (b, c) ELF maps of CO_2 adsorption on N-ZnO(101) with and without O_2 pre-adsorption, respectively. The bottom side views are corresponding adsorption structures. The red, gray, brown and white spheres correspond to O, Zn, C and N atoms, respectively (For interpretation of the references to colour in this figure legend, the reader is referred to the web version of this article).

Table 2
Calculated gas-slab interfacial distance ($d_{gas\text{-}slab}$), adsorption energy per gas molecule (E_{ads}), and Bader charge transfer per molecule on N-ZnO(101) slab and N-ZnO(101) slab pre-adsorbed with O_2.

Model	Adsorbate	d_{gas_slab} (Å)	E_{abs} (eV)	ΔQ (e)[1]
N-ZnO(101)	CO_2	1.35	-1.61	0.019
N-ZnO(101)	O_2	1.28	-3.50	-0.382
N-ZnO(101)-O_2	CO_2	6.22	-0.22	-0.001

[1] The higher resolution is applied due to small values.

during N_2 purge, as shown in Fig. 3(a).

3.3.3. *Bonding analysis of CO_2 adsorption on N-ZnO(101)*

To further illustrate the interaction between CO_2 and N-ZnO(101), the detailed DOS of N-ZnO(101) slab during CO_2 adsorption was calculated. The system before CO_2 adsorption is denoted as "isolated system" while the system after CO_2 adsorption it is denoted as "adsorbed system", respectively. The corresponding density of states of the two systems are shown in Fig. 7(a). The discrete CO_2 nonbonding orbitals of $1\pi_g$, $2\pi_u$ and $5\pi_g$ [33] become invisible and the density of states of the N dopant overlaps with the density of states of CO_2^{ads} after CO_2

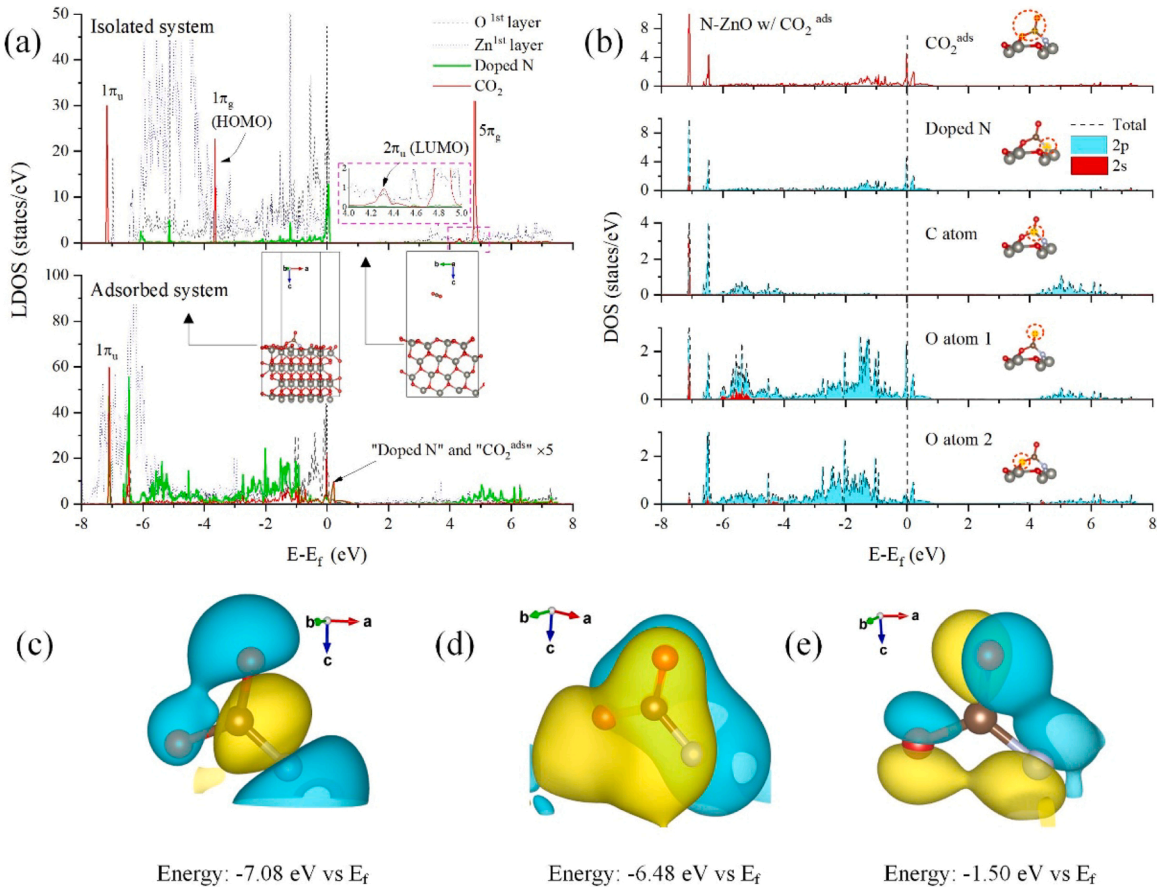

Fig. 7. DOS analysis of CO_2 adsorption on N-ZnO(101). (a) Local density of states. The insets are corresponding models of the calculated system. (b) LDOS of adsorbed CO_2, projected DOS of N dopant, and C and O of CO_2. The highlighted atoms in insets are corresponding atoms of the plotted PDOS. (c-e) Partial charge densities at the energies of − 7.08, − 6.48, and − 1.5 eV vs. E_f, respectively. The red, brown and white spheres correspond to oxygen, carbon and nitrogen atoms, respectively.

adsorption, which indicates strong interactions between the slab and the CO_2 molecule.

To understand the interactions between CO_2 and N dopant, the projected density of state (PDOS) of N and CO_2^{ads} are calculated and shown in Fig. 7(b). O_{atom1} and O_{atom2} denote the oxygen atoms, in O_2, further and closer to the surface, respectively. One can see that in the lower energy range, i.e. ∼ − 7 eV vs. Fermi energy (E_f), the 2 s/ 2p orbitals of C, O and N mix together to form sp hybrid orbitals. The planar structure of these four atoms (shown as insets) indicates the hybridization is sp^2 hybridization [34]. The partial charge decomposed from the calculated total wave function at − 7.08 eV is shown in Fig. 7(c) where a σ bond is seen to form between N/O and C atoms. It is probably the σ bonds of C-O and C-N that reshapes the structure of the CO_2 molecule after adsorption. The DOS overlapping peak at − 6.48 eV below E_f is the result of hybridization of N 2p, C 2p, O_{atom1} 2p, and O_{atom2} 2p orbitals, which appears as a new peak after CO_2 adsorption compared to the original DOS in Fig. 7(a). The corresponding partial charge density is shown in Fig. 7(d), which indicates there is a π bond among these 4 atoms. In the range near the Fermi energy, the N 2p orbital overlaps with two O 2p instead of the closest C atom. The corresponding partial charge density shown in Fig. 7(e) exhibits N dopant sharing positive and negative charges with two O atoms, respectively. It is probably an antibonding orbital of the π bond.

When pre-adsorbed with O_2, the N 2s/ 2p orbitals of N dopant in N-ZnO(101) mix with O 2s/2p of O_2 and the lone pair of the N dopant is saturated by adsorbed O_2. As a consequence, N 2s/2p of the N dopant are no longer able to interact with CO_2 (no overlapped DOS peaks can be found), as shown in Fig. S6.

Therefore, the N dopant, with the lone pair, acting as the Lewis acid, can interact with CO_2 (Lewis base) and form a σ bond (overlap of sp^2 hybrid orbitals) and a π bond (overlap of 2p orbitals). During orbital mixing, the occupied $1\pi_g$ orbital of CO_2 shares electrons with N 2p orbital to achieve charge transfer.

4. Conclusion

In summary, we have synthesized the well-connected ZnO nanoparticles network and confirmed crystal structures as well as surface chemical status. CO_2 gas sensing test has been performed in both N_2 and air background, exhibiting good short-term stability and reproducibility. Additionally, the response in N_2 background is significantly larger.

DFT calculations show N-doped ZnO(101) has the highest CO_2 adsorption energy among the four slabs examined (ZnO(101), V_O-ZnO (101), N-ZnO(101) and O-N-ZnO(101)). It is the only system where CO_2 serves as an electron donor during adsorption process, in agreement with the negative sensor response feature upon CO_2 exposure in the N_2 background. However, with pre-adsorbed O_2, CO_2 can no longer approach the surface of N-ZnO(101) ($d_{gas\text{-}slab}$ = 6.22 Å), which is believed to be the cause of the lower response in air background. Therefore, in combine with the higher CO_2 selectivity of the in-situ annealed material than the ex-situ counterpart, N doping is believed to be responsible for the CO_2 responses.

Further study concerning the CO_2 adsorption on N-ZnO(101) shows that CO_2 acts as a Lewis base while the N dopant acts as a Lewis acid during the adsorption process. The N sp^2 hybridized orbitals and N 2p orbitals mix with sp^2 hybridized orbital of C atom and 2p orbitals of C/O

atoms in CO_2, and form σ bonds and π bonds, respectively, which are responsible for chemisorption. When pre-adsorbed with O_2 for measurements in air, N 2s/ 2p orbitals mix with O 2s/ 2p orbitals of O_2 and CO_2 can no longer interact with the surface.

This contribution will not only expand the knowledge of CO_2 sensing, but also will guide design of new functional materials for CO_2 sensing or capture.

CRediT authorship contribution statement

Yong Xia: Conceptualization, Investigation, Experiments, Computation, Writing – original draft. **Aifei Pan:** Experiments, Computations, Writing – review & editing. **Ya-Qiong Su:** Computations, Writing – review & editing. **Sikai Zhao:** Writing – review & editing. **Zhou Li:** Writing – review & editing. **Adrian K. Davey:** Writing – review & editing. **Roya Maboudian:** Supervision,Writing – review & editing. **Carlo Carraro:** Conceptualization, Resources, Supervision, Writing – review & editing. **Libo Zhao:** Resources, Supervision, Writing – review & editing.

Declaration of Competing Interest

The authors declare that they have no known competing financial interests or personal relationships that could have appeared to influence the work reported in this paper.

Acknowledgements

The support of the U.S. National Science Foundation (grant # 1903188) and the industrial members of the Berkeley Sensor & Actuator Center is gratefully acknowledged. The characterization work at the Molecular Foundry is supported by Office of Science, Office of Basic Energy Sciences, of the U.S. Department of Energy under Contract No. DE-AC02-05CH11231. Y.X. acknowledges the help from Chunhui Xiao in calculations and additional support from Chinese Scholarship Council. L.Z. acknowledges the National Key Research & Development (R&D) Plan (2020YFB2009100), National Natural Science Foundation of China (51890884, U1909221), and the Shaanxi Province Natural Science Basic Research Project (2019JC-06).

Appendix A. Supporting information

Supplementary data associated with this article can be found in the online version at doi:10.1016/j.snb.2022.131359.

References

[1] A.K. Davey, X. Gao, Y. Xia, Z. Li, M.N. Dods, S. Delacruz, A. Pan, S. Swamy, D. Gardner, C. Carraro, R. Maboudian, Amine-functionalized metal-organic framework ZIF-8 toward colorimetric CO_2 sensing in indoor air environment, Sens. Actuators B Chem. 344 (2021), 130313.
[2] E. Levintal, K. Lee Kang, L. Larson, E. Winkelman, L. Nackley, N. Weisbrod, J. S. Selker, C.J. Udell, eGreenhouse: robotically positioned, low-cost, open-source CO_2 analyzer and sensor device for greenhouse applications, HardwareX 9 (2021), e00193.
[3] L.M. Calvo, R. Domingo, CO_2 emissions reduction and energy efficiency improvements in paper making drying process control by sensors, Sustainability 9 (2017) 514.
[4] L. Fleming, D. Gibson, S. Song, C. Li, S. Reid, Reducing N_2O induced cross-talk in a NDIR CO_2 gas sensor for breath analysis using multilayer thin film optical interference coatings, Surf. Coat. Technol. 336 (2018) 9–16.
[5] D.K.T. Ng, C.P. Ho, L. Xu, W. Chen, Y.H. Fu, T. Zhang, L.Y. Siow, N. Jaafar, E.J. Ng, Y. Gao, H. Cai, Q. Zhang, L. Lee, NDIR CO_2 gas sensing using CMOS compatible MEMS ScAlN-based pyroelectric detector, Sens. Actuators B Chem. 346 (2021), 130437.
[6] C. Schwandt, R.V. Kumar, M.P. Hills, Solid state electrochemical gas sensor for the quantitative determination of carbon dioxide, Sens. Actuators B Chem. 265 (2018) 27–34.
[7] K.K. Sappati, S. Bhadra, Temperature compensated differential acoustic sensor for CO_2 sensing, Meas. Sci. Technol. 32 (2021), 105103.
[8] T. Suzuki, A. Sackmann, A. Oprea, U. Weimar, N. Bârsan, Chemoresistive CO_2 gas sensors based On $La_2O_2CO_3$: sensing mechanism insights provided by operando characterization, ACS Sens. 5 (2020) 2555–2562.
[9] T. Suzuki, A. Sackmann, F. Lauxmann, C. Berthold, U. Weimar, N. Bârsan, CO_2 sensing with gas sensors based on rare-earth compounds: material exploration, Sens. Actuators B: Chem. 317 (2020), 128128.
[10] S. Joshi, S.J. Ippolito, S. Periasamy, Y.M. Sabri, M.V. Sunkara, Efficient heterostructures of Ag@ CuO/$BaTiO_3$ for low-temperature CO_2 gas detection: assessing the role of nanointerfaces during sensing by operando DRIFTS technique, ACS Appl. Mater. Interfaces 9 (2017) 27014–27026.
[11] N. Tanvir, O. Yurchenko, E. Laubender, R. Pohle, O. Sicard, G. Urban, Zinc peroxide combustion promoter in preparation of CuO layers for conductometric CO_2 sensing, Sens. Actuators B Chem. 257 (2018) 1027–1034, 1027-34.
[12] R. Dhahri, M. Hjiri, L. El Mir, E. Fazio, F. Neri, F. Barreca, N. Donato, A. Bonavita, S.G. Leonardi, G. Neri, ZnO: Ca nanopowders with enhanced CO_2 sensing properties, J. Phys. D Appl. Phys. 48 (2015), 255503.
[13] C.A. Zito, T.M. Perfecto, A.-C. Dippel, D.P. Volanti, D. Koziej, Low-temperature carbon dioxide gas sensor based on yolk–shell ceria nanospheres, ACS Appl. Mater. Interfaces 12 (2020) 17745–17751, 17745-51.
[14] Y. Xia, A. Pan, D.W. Gardner, S. Zhao, A.K. Davey, Z. Li, L. Zhao, C. Carraro, R. Maboudian, Well-connected ZnO nanoparticle network fabricated by in-situ annealing of ZIF-8 for enhanced sensitivity in gas sensing application, Sens. Actuators B Chem. 344 (2021), 130180.
[15] J. Hafner, Ab-initio simulations of materials using VASP: density-functional theory and beyond, J. Comput. Chem. 29 (2008), 2044-78.
[16] G. Kresse, J. Furthmüller, Efficient iterative schemes for ab initio total-energy calculations using a plane-wave basis set, Phys. Rev. B 54 (1996) 11169–11186.
[17] J.P. Perdew, K. Burke, M. Ernzerhof, Generalized gradient approximation made simple, Phys. Rev. Lett. 77 (1996) 3865–3868.
[18] N. Pueyo Bellafont, F. Viñes, W. Hieringer, F. Illas, Predicting core level binding energies shifts: suitability of the projector augmented wave approach as implemented in VASP, J. Comput. Chem. 38 (2017) 518–522.
[19] R.L. Freire, M.O. Orlandi, J.L. Da, Silva, Ab initio investigation of the role of charge transfer in the adsorption properties of H_2, N_2, O_2, CO, NO, CO_2, NO_2, and CH_4 on the van der Waals layered Sn_3O_4 semiconductor, Phys. Rev. Mater. 4 (2020), 104002.
[20] S. Grimme, J. Antony, S. Ehrlich, H. Krieg, A consistent and accurate ab initio parametrization of density functional dispersion correction (DFT-D) for the 94 elements H-Pu, J. Chem. Phys. 132 (2010), 154104.
[21] K. Momma, F. Izumi, VESTA 3 for three-dimensional visualization of crystal, volumetric and morphology data, J. Appl. Crystallogr. 44 (2011) 1272–1276.
[22] R. Bader, Atoms in molecule, A Quantum Theory, (1990).
[23] W. Tang, E. Sanville, G. Henkelman, A grid-based Bader analysis algorithm without lattice bias, J. Phys.: Condens. Matter 21 (2009), 084204.
[24] M. Schumm, ZnO-basedsemiconductors studied by Raman spectroscopy: semimagnetic alloying, doping,and nanostructures: Universität Würzburg; 2008.
[25] F. Friedrich, N. Nickel, Resonant Raman scattering in hydrogen and nitrogen doped ZnO, Appl. Phys. Lett. 91 (2007), 111903.
[26] D.N. Montenegro, V. Hortelano, O. Martínez, M.C. Martínez-Tomas, V. Sallet, V. Muñoz-Sanjosé, J. Jiménez, Non-radiative recombination centres in catalyst-free ZnO nanorods grown by atmospheric-metal organic chemical vapour deposition, J. Phys. D Appl. Phys. 46 (2013), 235302.
[27] Y. Chen, D. Wang, H. Qin, H. Zhang, Z. Zhang, G. Zhou, C. Gao, J. Hu, CO_2 sensing properties and mechanism of $PrFeO_3$ and $NdFeO_3$ thick film sensor, J. Rare Earths 37 (2019) 80–87.
[28] M. Wu, J. Shin, Y. Hong, D. Jang, X. Jin, H.-I. Kwon, J.H. Lee, An FET-type gas sensor with a sodium ion conducting solid electrolyte for CO_2 detection, Sens. Actuators B Chem. 259 (2018) 1058–1065.
[29] W.M. Haynes, CRC Handbook of Chemistry and Physics, CRC Press, Boca Raton, 2016.
[30] D. Chen, L. Powers, Synthesis and structures of $Zn(C_6H_{12}OS_2)_2(ClO_4)_2$ and $Zn(C_3H_6NS_2)_2(C_3H_4N_2)$—Model compounds for the Zn sites in RNA polymerase, J. Inorg. Biochem. 58 (1995) 245–253.
[31] Y. Wu, X. Chen, K. Weng, A. Arramel, N. Li, Highly sensitive and selective gas sensor using heteroatom doping graphdiyne: a DFT study, Adv. Electron. Mater. 7 (2021) 2001244.
[32] K. Koumpouras, J.A. Larsson, Distinguishing between chemical bonding and physical binding using electron localization function (ELF), J. Phys. Condens. Matter 32 (2020), 315502.
[33] A. Paparo, J. Okuda, Carbon dioxide complexes: bonding modes and synthetic methods, Coord. Chem. Rev. 334 (2017) 136–149, 136-49.
[34] T.L. Brown, Chemistry: the Central Science, Pearson Education, Boston, 2009.

Yong Xia is a Ph.D candidate in Xi'an Jiaotong University majoring in Instrument Science and Technology. He received his B. S. degree from Chang'an University in 2013. As a visiting student, he studied synthesis of nanomaterials for gas sensing application in University of California, Berkeley (2018.11–2020.12). His current research interest is micro-nanofabrication for bio-chemical sensors.

Aifei Pan is a Ph.D candidate in Xi'an Jiaotong University majoring in mechanical engineering. As a visiting student in UC Berkeley under the supervision of Prof. Maboudian and Prof. Carraro, she studied MOFs-enhanced SERS based chemical sensing.

Ya-Qiong Su is professor in Xi'an Jiaotong University, majoring in Chemistry Engineering. His research focuses on computation chemistry for catalysts design and energy applications.

Sikai Zhao received his M.S. degree from Northeastern University, China, in 2017 and presently is a Ph.D. student in the School of Resources and Civil Engineering, Northeastern University, China. His current research interests include gas sensors, low-dimensional and composite nanomaterials.

Zhou Li is a Ph.D. candidate of State Key Laboratory of Fire Science, University of Science and Technology of China. His research interest is mainly on metal oxide semiconductor gas sensors. Currently, he works as a visiting graduate researcher under the supervision of Prof. Roya Maboudian in the Department of Chemical and Biomolecular Engineering at University of California, Berkeley.

Adrian K. Davey is a Ph.D candidate in UC Berkeley since 2018. He received his B.S. form University of Maryland, Baltimore County (UMBC) majoring Chemical Engineering, in 2018. His current interest is the use of metal-organic frameworks toward colorimetric analyte sensing.

Libo Zhao was born in Yantai, China, in 1978. He received M.S. degree in Instrument Science and Technology in 2003 and Ph.D. degree in Instrument Science and Technology in 2007, both from Xi'an Jiaotong University, Xi'an, China. He is currently working as a professor in Xi'an Jiaotong University. His research interests include micro and nano-fabrication technology, MEMS sensor technology and precision machining technology.

Roya Maboudian is a Professor of chemical engineering at the University of California, Berkeley. She received her pH.D. in applied physics from California Institute of Technology. Her current research interests are in the areas of surface/interfacial science and engineering of micro-/nanosystems, and thin-film science and technology.

Carlo Carraro is an adjunct professor in the Department of Chemical and Biomolecular engineering at the University of California, Berkeley. He received his bachelor's degree from the University of Padua, Padua, Italy, and his pH.D. degree from California Institute of Technology in Pasadena, California. His research interests are in the physics and chemistry of surfaces and synthesis of novel thin-film materials and processes.